J. Am. Chem. Soc. **1994,** *116,* 154–161

Rationalization and Prediction of Rare Earth Selenide Superstructures

Stephen Lee[*] and Brendan Foran

Contribution from the Willard H. Dow Laboratories, Department of Chemistry, University of Michigan, Ann Arbor, Michigan 48109-1055

Received July 30, 1993. Revised Manuscript Received October 4, 1993[⊛]

Abstract: We apply second-moment scaled Hückel theory with inclusion of ionic terms to rationalize or predict superstructures found in elemental selenium, LnQ_2 (Ln = La, Ce; Q = S, Se), $Ln_{10}Se_{19}$ (Ln = La, Ce, Pr, Nd, Sm), and $RbDy_3Se_8$. All these structures contain distortions of square lattices of chalcogen atoms. In the case of $Ln_{10}Se_{19}$ and $RbDy_3Se_8$ these lattice distortions are coupled to ordered defects in the chalcogen square lattice. On the basis of our energy calculations we propose eight ground state $RbDy_3Se_8$ superstructure patterns among the 5×10^5 possible alternatives. Finally we explain the results of our calculations using HOMO–LUMO and Madelung energy arguments.

Introduction

One difficult problem in X-ray crystallography is the accurate solution of crystal superstructures. The crystallographer is frequently hampered by weak to exceedingly weak reflections, by poor statistics, and in many cases by crystal twinning as well. Indeed, the resolution of crystal superstructures often requires a good initial model as the basis for further refinement. At the same time the resolution of superstructures is essential for the understanding of the properties of given materials.[1] This is particularly true for metals and intermetallic compounds where the crystalline superstructure provides key information about the overall electronic structure.

In this paper we consider the use of a simple quantum mechanical method to help resolve such problems for several near-metallic selenide phases. In particular we use a method of calculation which has been found useful in the rationalization of metal and near-metal structures.[2] We call this method second-moment scaling, as it involves an approximate form of interatomic repulsions based on the second moment of the one-electron density of states (i.e., in molecular terms of the one-electron molecular orbital diagram). This method has allowed for the rationalization of the Hume–Rothery electron concentration rules for transition metal and noble metal alloys, the optimization of both metallic and nonmetallic elemental structures, and the rationalization of the structures of several families of intermetallic compounds. Applications of this method are generally limited to highly covalent or metallic bonds. We apply this technique here to rare earth polyselenides which generally contain superstructures of an infinite square lattice.[3] We show in the case of both small and large unit cell superstructures that the energies derived by the second-moment scaled Hückel Hamiltonian, coupled (where applicable) with a simple ionic model to describe the electropositive metal–selenium interactions, can correctly identify the experimentally observed superstructures. Examples include elemental selenium itself, the $LaSe_2$ (or $CeSe_2$) structure, and the $Ln_{10}Se_{19}$ (Ln = La, Ce, Pr, Nd, and Sm) structure.[4] We show that in each case that, up to a specified-size unit cell, the true experimental structure corresponds to an energetic global minimum of our energy expression. We then turn to the $RbDy_3Se_8$ structure as an example of superstructure which has not been resolved by traditional single-crystal X-ray studies.[5] We deduce from our calculations a small number of chemically reasonable alternatives for the full crystal structure of this final phase. Finally, we discuss the underlying features responsible for the stability of these phases and their accompanying superstructures.

Experimental Selenium

The ambient-temperature and -pressure structure of elemental selenium is a distortion of the simple cubic structure, as is shown

---

[*] Author to whom correspondence should be sent.

[⊛] Abstract published in *Advance ACS Abstracts,* December 15, 1993.

(1) Problems with superstructure are prevalent in much of intermetallic and alloy chemistry. Examples of superstructures, both those fully resolved and those only partially resolved, include for rare earth chalcogenides: (a) Wang, R.; Steinfink, H. *Inorg. Chem.* **1967**, *6* (9), 1685. (b) Benazeth, S.; Carré, D.; Guittard, M.; Flahaut, J. *C. R. Acad. Sci. Paris, Serie C* **1975**, *280*, 1021. $ThSi_2$ types: (c) Schobinger-Papamantellos, P.; Buschow, K. H. J.; Janssen, T. *Phase Transitions*, **1993**, *33*, 133. (d) Schobinger-Papamantellos, P.; Buschow, K. H. J.; Fischer, P. *J. Magn. Magn. Mater.* **1991**, *97*, 53. (e) Lambert-Andron, B.; Houssay, E.; Madar, R.; Hippert, F.; Pierre, J.; Auffret, S. *J. Less-Common Met.* **1990**, *167*, 53. (f) Auffret, S.; Pierre, J.; Lambert, B.; Soubeyroux, J. L.; Chroboczek, J. A. *Physica* **1990**, *B162*, 271. (g) Pierre, J.; Lambert-Andron, B.; Soubeyroux, J. L. *J. Magn. Magn. Mater.* **1989**, *81*, 30. (h) Bruskov, V. A.; Bodak, O. I.; Pecharskii, V. K.; Gladyshevskii, E. I.; Muratova, L. A. *Sov. Phys.—Crystallogr.* **1983**, *28*, 260. (i) Madar, R.; Houssay, R.; Rouault, A.; Senateur, J. P.; Lambert, B.; Meneau d'Anterroches, C.; Pierre, J.; Laborde, O.; Soubeyroux, J. L.; Pelisser, J. *J. Mater. Res.* **1990**, *5*, 2126. (j) Lee, W. H.; Shelton, R. N.; Dhar, D. K.; Gschneidner, K. A., Jr. *Phys. Rev. B* **1987**, *35*, 8523. (k) Yashima, H.; Satoh, T.; Mori, H.; Watanabe, D.; Ohtsuka, T. *Solid State Commun.* **1982**, *41*, 1. Alloys: (l) Morton, A. J. *Acta Metall.* **1979**, *27*, 863. (m) Meulemans, M.; Delavignette, P.; Garcia-Gonzales, F.; Amelinckx, S. *Mater. Res. Bull.* **1970**, *5*, 1025. (n) Johansson, A.; Ljung, H.; Westman, S. *Acta Chem. Scand.* **1968**, *22*, 2743. (o) Nover, G.; Schubert, K. *J. Less-Commun. Met.* **1980**, *75*, 51. Oxides and sulfides: (p) Hyde, B. G.; Bevan, D. J. M.; Eyring, L. *Philos. Trans. R. Soc. London* **1966**, *A259*, 583. (q) Jellinek, F. *Acta Crystallogr.* **1957**, *10*, 620.

(2) (a) This method was proposed independently for AB (main group–transition metal) (Pettifor, D. G.; Podloucky, R. *Phys. Rev. Lett.* **1984**, *53*, 1080) and for the Peierls distortion (Burdett, J. K.; Lee, S. *J. Am. Chem. Soc.* **1985**, *107*, 3063). Other papers whose results are based on this method: (b) Pettifor, D. G. *J. Phys. C.* **1986**, *19*, 285. (c) Cressoni, J. C.; Pettifor, D. G. *J. Phys.: Condens. Matter* **1991**, *3*, 495. (d) Lee, S. *J. Am. Chem. Soc.* **1991**, *113*, 101; **1991**, *113*, 8611. (e) Hoistad, L. M.; Lee, S.; Pasternak, J. *J. Am. Chem. Soc.* **1992**, *114*, 4790. (f) Hoistad, L. M.; Lee, S. *J. Am. Chem. Soc.* **1991**, *113*, 8216. (g) Lee, S. *Acc. Chem. Res.* **1991**, *24*, 249. (h) Lee, S. *Inorg. Chem.* **1992**, *31*, 3063. (i) Lee, S.; Hoistad, L. M.; Carter, S. T. *New J. Chem.* **1992**, *16*, 651. (j) Lee, S.; Roussean, R.; Wells, C. *Phys. Rev.* **1992**, *46*, 12121.

(3) (a) Haase, D. J.; Steinfink, H.; Weiss, E. *J. Inorg. Chem.* **1965**, *4*, 538. (b) Ramsey, T. H.; Steinfink, H.; Weiss, E. *J. Inorg. Chem.* **1965**, *4*, 1154. (c) Bucher, E.; Andres, K.; DiSalvo, F. J.; Maita, J. P.; Gossard, A. C.; Cooper, A. S.; Hull, G. W. *Phys. Rev. B* **1975**, *II*, 500. (d) Wang, R.; Steinfink, H.; Bradley, W. F. *Inorg. Chem.* **1966**, *5*, 142. (e) Norling, B. K.; Steinfink, H. *Inorg. Chem.* **1966**, *5*, 1988. (f) Pardo, M.-P.; Gorochev, O.; Flahaut, J.; Domange, L. *C. R. Acad. Sci. Paris* **1965**, *260*, 1666. (g) Pardo, M.-P.; Flahaut, J. *Bull. Soc. Chim. Fr.* **1967**, *10*, 3658. (h) Lin, W.; Steinfink, H.; Weiss, E. J. *Inorg. Chem.* **1965**, *4*, 877. (i) The square lattice has been discussed from a theoretical viewpoint in: Tremel, W.; Hoffmann, R. *J. Am. Chem. Soc.* **1987**, *109*, 124.

(4) (a) Se_2^{2-} formation in $CeSe_2$: Marcon, J.-P.; Pascard, R. *C. R. Acad. Sci. Paris* **1968**, *266*, 270. (b) Se_2^{2-} formation in $LaSe_2$: Bénazeth, S.; Carré, D.; Laruelle, P. *Acta Crystallogr.* **1982**, *B38*, 33. (c) $LaSe_{2-x}$ superstructures: Bénazeth, S.; Carré, D.; Guittard, M.; Flahaut, J. *C. R. Acad. Sci. Paris* **1975**, *280*, 1021. (d) $LaSe_{1.9}$: Grupe, M.; Urland, W. J. *Less-Commun. Met.* **1991**, *170*, 271. (e) $CeSe_{1.9}$ and $PrSe_{1.9}$: Plambeck-Fischer, P.; Abriel, W.; Urland, W. *J. Solid State Chem.* **1989**, *78*, 164.

(5) Foran, B.; Lee, S.; Aronson, M. *Chem. Mater.* **1993**, *5*, 974.

0002-7863/94/1516-0154$04.50/0

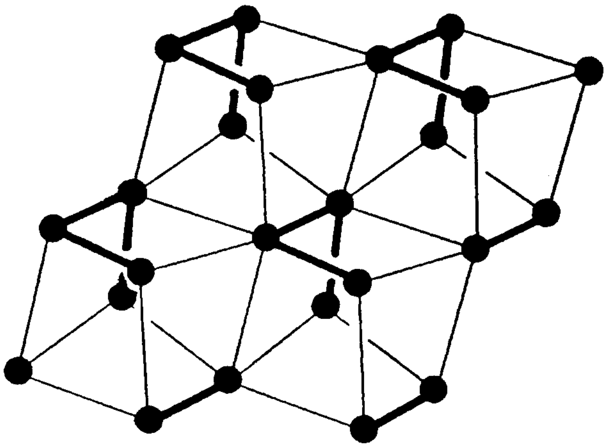

Figure 1. Structure of elemental selenium.

in Figure 1. This distortion creates helices of selenium atoms which in Figure 1 run perpendicular to the plane of the page.[6] The origin of this distortion has been extensively studied and is well understood.[7] It may be viewed as a three-dimensional version of the Peierls distortion in which the original six nearest neighbors of the simple cubic structure have now been distorted into two first-nearest neighbors at 2.37 Å and four second-nearest neighbors at 3.44 Å. The observed selenium structure is trigonal with three atoms in the unit cell located at $(x, 0, {}^1/_3)$, $(0, x, {}^2/_3)$, and $(-x, -x, 0)$, $x = 0.2254$, with a cell axis c/a ratio of 1.136. Heavier elements in the chalcogen series have the same basic structure. For elemental tellurium $x = 0.2633$ and c/a = 1.330 while for elemental polonium $x = {}^1/_3$ and c/a = 1.225. These latter values correspond to the undistorted simple cubic lattice, and in parallel with the Peierls distortion model, polonium is a metal.[6b] We thus have the trend that as we go to heavier chalcogen atoms, the ratio between second- and first-nearest neighbor distances is ever decreasing; from selenium to tellurium to polonium this ratio changes from 1.45 to 1.23 to 1.00.

In this section we wish to account for this distortion within the tight-binding scheme on which our energy calculations are based. The tight-binding method relies on atomic parameters which determine both the energies of the specific atomic orbitals and the radial form of the atomic wave functions.[8] As we have noted elsewhere, in most cases we can use extended Hückel or Hartree–Fock atomic parameters for these values.[3b,9] One exception is in the case of contracted valence orbitals, where highly contracted orbitals must be used. This is precisely the situation in heavier main group elements (such as tellurium and polonium) where relativistic effects lead to contraction of the valence s-orbitals.[10] This relativistic contraction is known to be responsible for the inert-pair effect in heavy main group atoms as well as the 90° bond angles found in heavy main group atom hydrides. In previous work we have shown how contraction of the s-orbital can be used to account for the structures of heavy main group atoms such as the face-centered cubic structure of thallium and the unusual white form of tin.[2d]

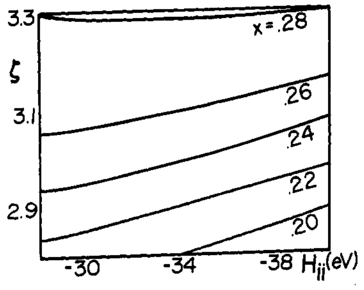

Figure 2. Contour map of the optimal value of the atomic positional parameter x for given values of the 4p-orbital Coulombic integral, H_{ii}, and Slater exponent, ζ.

We have therefore undertaken a parallel study for the heavy chalcogen atoms. In particular we find by a method of steepest descent the minimum-energy structure for a given value of the s-orbital parameters. We use Slater-type orbitals (STO) with a single ζ expansion for which more contracted orbitals have larger ζ values. As the s-orbitals contract, the energy of the s-orbitals, as represented by the Hückel Coulombic integrals (H_{ii}), also goes to lower values. For the sake of simplicity we have kept the valence p-orbital at the same parameter values for all calculations. Off-diagonal matrix elements are calculated using the Wolfsberg–Helmholz approximation.[11]

In Figure 2 we show a contour map plotting the optimal value of the atomic positional parameter x for a given Slater exponent, ζ, and Hückel Coulombic integral, H_{ii}. It may be seen that x increases in a steady fashion as ζ reaches higher, more contracted values. For very contracted ζ values, $x = {}^1/_3$. This functional dependence is of particular interest, as the x value can serve as an order parameter measuring the metallic or insulating character of the phase. For $x = {}^1/_3$ there are six equidistant nearest neighbors and the overall structure is metallic. For $x < {}^1/_3$ there are two closest nearest neighbors and four more distant second-nearest neighbors and the structure correspondingly shows loss of its metallic character. From comparison to the known experimental data, elemental tellurium (where $x = 0.263$) is closer to the metallic state than is elemental selenium (where $x = 0.225$). As Figure 2 shows, we find appropriate ζ values to be near 2.9 for elemental selenium and near 3.1 for elemental tellurium. The s-orbital contraction thus accounts for changes in structures among the heavier chalcogenides just as it did in our earlier study on group 13–15 elemental structures.[2d] In the remainder of this paper we use $\zeta(4s) = 2.9$ and $H_{ii}(4s) = -32.0$ eV as our selenium s-orbital parameters. This H_{ii} value leads to an optimal c/a ratio close to the experimentally observed value (c/a = 1.132 (theory) vs 1.136 (expt)). This rather low value of H_{ii} is in keeping with the use of the Hückel vs the extended-Hückel model.[2g]

$LaSe_2$ Structure Type

The $LaSe_2$ structure, a distorted version of the anti-Cu_2Sb structure type, is illustrated in Figure 3a.[3] The anti-Cu_2Sb structure may be conveniently viewed as a tetragonal layer structure with planar four-coordinate square lattices of selenium atoms interlayered with sheets of distorted cubes are rare earth and selenium atoms. This latter cubic motif is a distorted form of that found for the rock-salt monochalcogenides. There are therefore two types of selenium atoms in the Cu_2Sb structure type. The first are the selenium atoms in the infinite square sheets which have four in-plane selenium neighbors at a distance

---

(6) (a) Donohue, J. *The Structure of the Elements*; J. Wiley: New York, 1974; Chapter 9, p 317. (b) Young, D. A. *Phase Diagram of the Elements*; University of California Press: Berkeley, CA, 1991.

(7) (a) Peierls, R. E. *Quantum Theory of Solids*; Oxford University Press: Oxford, U.K., 1955. (b) Burdett, J. K.; Lee, S. *J. Am. Chem. Soc.* **1983**, *105*, 1079.

(8) For a discussion of these ideas, see: (a) Burdett, J. K. *Molecular Shapes*; J. Wiley: New York, 1980. (b) Gimarc, B. M. *Molecular Structure and Bonding*; Academic Press: New York, 1979.

(9) (a) Clementi, E.; Roetti, C. *At. Data Nucl. Data Tables* **1974**, *14*, 177. (b) Mann, J. B. *Atomic Structures Calculations, 1: Hartree–Fock Energy Results for Elements Hydrogen to Lawrencium*; Clearinghouse for Technical Literature: Springfield, MA, 1967. (c) Many important atomic parameters are used and discussed in: Hoffmann, R. *J. Chem. Phys.* **1963**, *39*, 1397. (d) Anderson, A. B.; Hoffmann, R. *J. Chem. Phys.* **1974**, *60*, 4271. (e) Rossi, A. R.; Hoffmann, R. *Inorg. Chem.* **1975**, *97*, 4884. (f) Elian, M.; Hoffmann, R. *Inorg. Chem.* **1975**, *14*, 1058. (g) Summerville, R. H.; Hoffmann, R. *J. Am. Chem. Soc.* **1976**, *98*, 7240. (h) Lauher, R. H.; Hoffmann, R. *J. Am. Chem. Soc.* **1976**, *98*, 1729. (i) Komiya, S.; Albright, T. A.; Hoffmann, R. *Inorg. Chem.* **1978**, *17*, 126. (j) Hughbanks, T.; Hoffmann, R.; Whangbo, M.-H.; Stewart, K.; Eisenstein, O.; Canadell, E. *J. Am. Chem. Soc.* **1982**, *104*, 3876. (k) Thorn, D.; Hoffmann, R. *Inorg. Chem.* **1978**, *17*, 126.

(10) (a) Pitzer, K. S. *Acc. Chem. Res.* **1979**, *12*, 271. (b) Pykkö, P.; Desclaux, J.-P. *Acc. Chem. Res.* **1979**, *12*, 276. (c) Lohr, L. L., Jr.; Pykkö, P. *Chem. Phys. Lett.* **1979**, *62*, 333.

(11) Wolfsberg, M.; Helmholz, L. *J. Chem. Phys.* **1957**, *20*, 83.

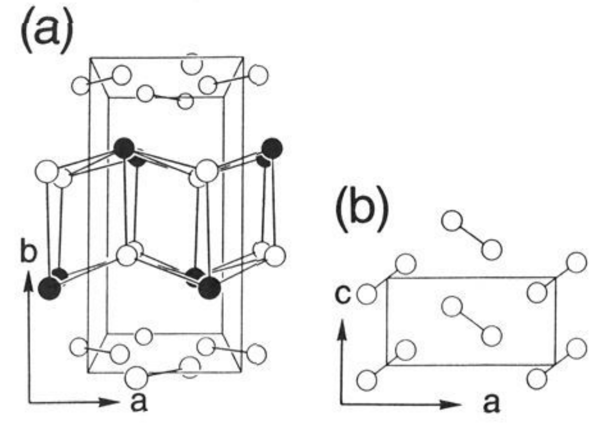

Figure 3. (a) $LaSe_2$ structure. (b) Herringbone pattern of dimers in the selenium sheet of $LaSe_2$.

of roughly 2.8 Å and an additional four out-of-plane rare earth neighbors (two in the layer above and two in the layer below) at a distance of roughly 3 Å. There is an equal number of a second type of selenium atom which lies in the cubic layer motif. These latter atoms have no near-selenium neighbors and hence make only five ionic bonds with the rare earth atoms. From these facts we may deduce that the oxidation states of the first and second types of selenium atoms are respectively –I and –II. The structure with undistorted square coordinate chalcogen sheets has been reported for several rare earth ditellurides.[12] As in the case of the elemental chalcogen structures, the undistorted lattice corresponds to the metallic state, thus making these structures 2-D metals (as the more ionic rare earth chalcogen layers are insulating).[13]

The $LaSe_2$ structure is a distortion of the above structure with the selenium atoms of the first type distorted from the initial square sheet location so as to generate Se_2^{2-} dimers. The short Se–Se bonds are 2.45-Å long while the three remaining Se–Se distances range from 3.1 to 3.4 Å. The formation of such dimers may be readily understood by application of the octet rule. (The octet rule requires each Se(–I) to form one Se–Se bond in order to generate eight electrons around each Se(–I) atom.) Of greater interest is the relative orientation of these dimers. The Se_2^{2-} dimers form a herringbone pattern illustrated in Figure 3b. This same herringbone pattern has been reported for CeS_2, LaS_2, and $CeSe_2$.[4]

We wish to show how, by a calculational method, one can anticipate the herringbone pattern found in $LaSe_2$. We model the energies in the $LaSe_2$ system as the sum of ionic energy caused by the La(III), Se(–I), and Se(–II) lattice and covalent-metallic energy which is the result of Se–Se interactions. We call these energies respectively E_{ion} and E_{cov}. Both E_{ion} and E_{cov} are the sum of repulsive and attractive energies where we take

$$E_{ion} = \sum_{i>j} \frac{q_i q_j}{r_{ij}} A + \sum_{c,a} \left(\frac{1}{r_{ca}}\right)^{m_{ca}} B \tag{1}$$

$$E_{cov} = \int_{-\infty}^{E_F} E\rho(E)\,dE + \gamma \int_{-\infty}^{\infty} E^2 \rho(E)\,dE \tag{2}$$

$$E_{tot} = E_{ion} + E_{cov} \tag{3}$$

where q_i is the formal charge on the ith atom, $\rho(E)$ is the Hückel or tight-binding density of states, E_F is the Fermi energy (the energy of the HOMO), and m_{ca}, A, B, and γ are constants. In particular m_{ca} depends on the average principal quantum number of the cation, c, and the anion, a. B is based on equilibrium data for LaSe in the rock-salt structure.[14] The first term on the right side of eq 1 is the ionic Coulombic energy which is calculated using the Ewald method.[15] The determinations of B and m_{ca} are standard.[16] As the repulsive energy, described by the second term on the right side of eq 1, is short-ranged, we consider only anion–cation interactions here. The remaining short-range repulsions generated by the close selenium neighbors are placed in the repulsive energy of E_{cov}. For E_{cov} we carry out a band calculation on only the selenium atoms. We assume the rare earth atoms have each donated three electrons to the various Se p-bands. To ensure numerical accuracy in the integration over k-space, the energies at a fairly large number of k-points were evaluated. In the case of $LaSe_2$ structural alternatives, this number varied between 100 and 300 points. We couple this method to a steepest descent algorithm. As we are interested in distortions of the square-sheet motifs, we allow only atoms within the square sheets to shift to lower energy conformations.

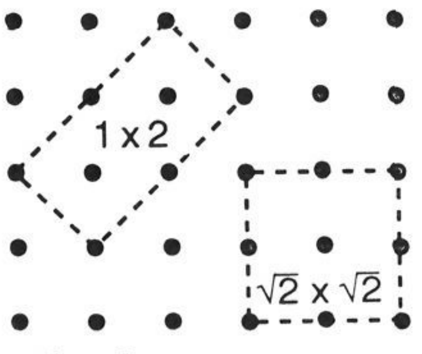

Figure 4. 1×2 and $\sqrt{2} \times \sqrt{2}$ unit cells for the selenium sheets in $LaSe_2$.

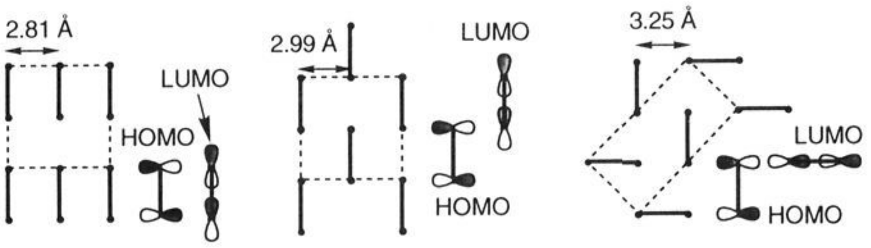

Figure 5. Local energy minimum structures for alternative $LaSe_2$ supercells.

Finally it should be noted that our energy expressions for both E_{cov} and E_{ion} are highly approximate. Furthermore, while recent studies have explored the accuracy of E_{cov}, it is well-known that the standard Born model is not a good indicator of observed crystal structure[17] for distorted geometries. In the case of the rare earth polyselenides however, the driving force for distortion is the propensity of selenium atoms to create covalent two-electron two-center and three-center four-electron bonds. These forces are modeled by the covalent selenium–selenium interactions of E_{cov}. However, without E_{ion} we do not get the correct structure.

Initially, we form unit cells of the undistorted anti-Cu_2Sb structure whose cell volume is 2 times greater than that of the primitive Cu_2Sb cell. We consider only supercells with increased a and b dimensions, as our interest is in the distortion of the square selenium sheets. There are only two such cells, both illustrated in Figure 4. The names for the two forms, 1×2 and $\sqrt{2} \times \sqrt{2}$ refer to the new supercell axis lengths in terms of the original Cu_2Sb cell. As in our calculations for elemental selenium, we find by a method of steepest descent the energy minima of the selenium lattice. In the case of $\sqrt{2} \times \sqrt{2}$ there were two minima, illustrated in Figure 5. We give these two minima sublabels of 1 and 2 to differentiate them (i.e., $\sqrt{2} \times \sqrt{2}$.1 and $\sqrt{2} \times \sqrt{2}$.2). Finally we found only one new minimum for the 1×2 cell. This latter superstructure is the same as the herringbone pattern found in $LaSe_2$. Both E_{ion} and E_{cov} are listed in Table 1 for these three energy minima. It may be seen that the 1 ×

---

[12] An early report of undistorted rare earth polychalcogenides was given in: Norling, B. K.; Steinfink, H. *Inorg. Chem.* **1966**, *5*, 1488.

[13] Clear two-dimensional conductivity has been recently shown in $SmTe_3$ and Sm_2Te_5. DiMasi, E.; Aronson, M.; Foran, B.; Lee, S. To be submitted.

[14] Crystallographic data for LaSe is taken from: Villars, P.; Calvart, L. D. *Pearson's Handbook of Crystallographic Data for Intermetallic Phases*; American Society of Metals, Metals Park, OH, 1985.

[15] See discussion in: Kittel, C. *Introduction to Solid State Physics*; J. Wiley: New York, 1986; p 606.

[16] See discussion in: Phillips, C. S. G.; Williams, R. J. P. *Inorganic Chemistry*; Oxford University Press: New York, 1965; p 146.

[17] See for example the discussion in: (a) Burdett, J. K.; Hughbanks, T. *Inorg. Chem.* **1985**, *24*, 1741. (b) Burdett, J. K.; Mitchell, J. *Chem. Mater.*, submitted for publication.

Table 1. Local Minima for $LaSe_2$ Stoichiometry

type	E_{tot} (eV)	E_{cov} (eV)	E_{ion} (eV)
1×2^a	-1401.04	-1171.37	-229.67
$\sqrt{2} \times \sqrt{2}.2$	-1400.06	-1170.87	-229.19
$\sqrt{2} \times \sqrt{2}.1$	-1397.07	-1168.90	-228.17

[a] $LaSe_2$ structure type.

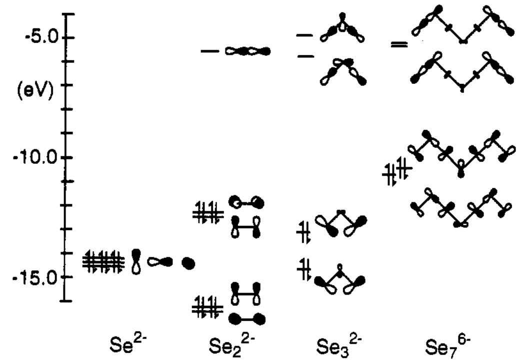

Figure 6. Pertinent molecular orbitals for selenium oligomers.

2 solution is 1 eV/unit cell lower in energy than either of the two $\sqrt{2} \times \sqrt{2}$ cells. Furthermore, both E_{ion} and E_{cov} are lowest in the 1×2 structure.

This energetic stability may be simply understood. We consider first E_{ion}. The ionic energy is in general minimized when the anions (the only atoms free to move in our optimization) are as far apart from each other as possible. Indeed, in the absence of E_{cov}, E_{ion} would favor a perfect undistorted square lattice of the free selenium atoms. Due to E_{cov} however, the selenium atoms do distort, and in accordance with the octet rule the selenium(-I) atoms dimerize into Se_2^{2-} pairs. E_{ion}, within the constraint of adhering to the octet rule scheme, is minimized when these Se_2^{2-} dimers lie as far apart from each other as possible. The shortest interdimer distances for the $\sqrt{2} \times \sqrt{2}.1$, $\sqrt{2} \times \sqrt{2}.2$, and 1×2 solutions are respectively 2.81, 2.99, and 3.25 Å. These distances correlate to their respective ionic energies of -201.09, -201.86, and -202.44 eV. It may be seen that there is a direct correlation between interdimer distances and the total ionic energy. The 1×2 structure therefore has a significantly lower E_{ion}.

We now turn to E_{cov}. As is well-known, it is generally the HOMO (highest occupied molecular orbital) to LUMO (lowest unoccupied molecular orbital) interactions which are responsible for the relation between E_{cov} and molecular geometry.[8] In Figure 6 we illustrate the HOMO and LUMO orbitals for the Se_2^{2-} dimer. It may be seen that there is only one unoccupied molecular orbital, a Se-Se σ^*-antibonding orbital. The HOMO orbitals are π^*-antibonding orbitals. We conclude HOMO-LUMO Se_2^{2-} interactions will be strongest when neighboring Se_2^{2-} dimers are perpendicular to one another. It may be seen that in the case of the 1×2 structure neighboring dimers are indeed perpendicular to one another. By contrast in the $\sqrt{2} \times \sqrt{2}.1$ structure, in which all Se_2^{2-} dimers are parallel to one another, there is no HOMO-LUMO interaction at all (indeed there are only energetically useless HOMO-HOMO and LUMO-LUMO interactions). Finally in the case of the $\sqrt{2} \times \sqrt{2}.2$ structure, the intermediate situation exists with some HOMO-LUMO and some HOMO-HOMO/LUMO-LUMO interactions. It is for this reason that E_{cov} is lowest for the 1×2 structure.

We conclude that the herringbone $LaSe_2$ pattern (the 1×2 cell) has optimized both its covalent and ionic forces. Indeed in the presence of E_{cov} alone, it would still be the favored structural alternative. This is experimentally observed. Elemental chlorine, bromine and iodine are isoelectronic with the sheets of Se(-I) and have this herringbone pattern.[18]

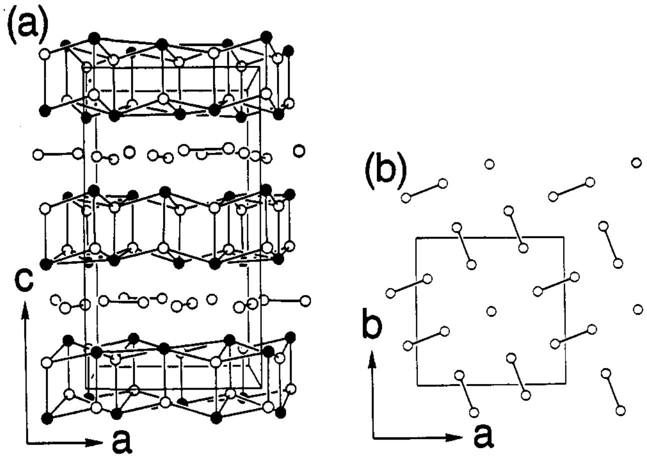

Figure 7. (a) $La_{10}Se_{19}$ structure. (b) Distortion pattern for the selenium sheet of $La_{10}Se_{19}$.

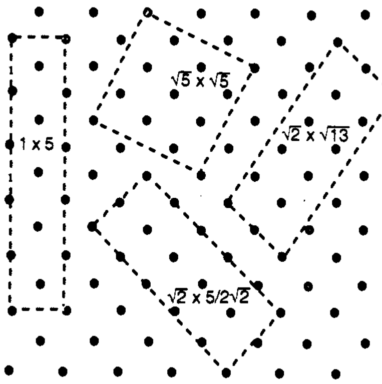

Figure 8. Four possible unit cells for the selenium sheet compatible with $La_{10}Se_{19}$ stoichiometry.

$La_{10}Se_{19}$ Structure Type

The $La_{10}Se_{19}$ structure is an ordered-defect Cu_2Sb structure (discussed in the previous section) where one-tenth of the atoms in the selenium square sheets have been removed. It has been observed for $Ln_{10}Se_{19}$ (Ln = La, Ce, Pr, Nd, Sm). The average oxidation state of the atoms in the selenium square sheet is -1.11. This corresponds to one Se(-II) atom per eight Se(-I) atoms. It is therefore quite reasonable that the square sheets should distort so as to fashion one isolated Se^{2-} atom per four Se_2^{2-} dimers. This is experimentally observed. We show this crystal structure in Figure 7. Both La-Se and Se-Se bond distances are comparable to those discussed in the previous section for $LaSe_2$.

To rationalize this structure, we use the same energetic model as in the previous section. Again, we wish to find the lowest energy structure up to a fixed unit cell size. We chose to consider all cells compatible with the Cu_2Sb structure type which contain exactly nineteen selenium atoms per primitive cell (in keeping with the $La_{10}Se_{19}$ stoichiometry). Again, we consider only superstructures in the *a*-*b* plane of the Cu_2Sb substructure. There are only four unit cells compatible with these requirements. These are illustrated in Figure 8. Cell dimensions for the four supercells are 1×5, $\sqrt{5} \times \sqrt{5}$, $\sqrt{2} \times 5\sqrt{2}/2$, and $\sqrt{2} \times \sqrt{13}$ times the size of the original Cu_2Sb cell. By a method of steepest descent (where we allow only the square-sheet selenium atoms to shift position), we found respectively one, three, one, and four local minima. Six of these are significantly lower in energy than the others. These six lowest energy structures all contain only Se_2^{2-} dimers and Se^{2-} monomers. The square-sheet selenium atoms have distorted to form four dimers for every monomer, in keeping with the octet rule. These six structures are illustrated in Figure

---

[18] Donohue, J. *The Structure of the Elements*; J. Wiley: New York, 1974; Chapter 10.

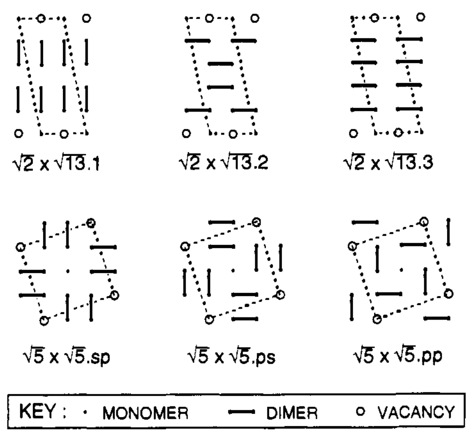

Figure 9. Local energy minimum structures for the alternative $La_{10}Se_{19}$ supercells.

Table 2. Local Minima for $La_{10}Se_{19}$ Stoichiometry

type	E_{tot} (eV)	E_{cov} (eV)	E_{ion} (eV)
$\sqrt{5}\times\sqrt{5}$.sp^a	-3371.44	-2789.60	-581.84
$\sqrt{5}\times\sqrt{5}$.pp	-3369.36	-2789.24	-580.12
$\sqrt{2}\times\sqrt{13}$.2	-3369.12	-2788.72	-580.40
$\sqrt{5}\times\sqrt{5}$.ps	-3367.20	-2787.50	-579.70
$\sqrt{2}\times\sqrt{13}$.3	-3365.88	-2786.84	-579.04
$\sqrt{2}\times\sqrt{13}$.1	-3365.16	-2785.71	-579.45

^{a} $LaSe_2$ structure type.

9. Three of them have $\sqrt{2}\times\sqrt{13}$ primitive unit cell dimensions, and the remainder are of $\sqrt{5}\times\sqrt{5}$ type. Each of the $\sqrt{2}\times\sqrt{13}$ primitive unit cells is half of an end-centered orthorhombic cell. To differentiate them we call the solutions $\sqrt{2}\times\sqrt{13}$.1, $\sqrt{2}\times\sqrt{13}$.2, and $\sqrt{2}\times\sqrt{13}$.3. In a similar fashion there are three $\sqrt{5}\times\sqrt{5}$ structures; each contains a four-fold rotation axis but no mirror planes in the *a* or *b* directions. We distinguish between these $\sqrt{5}\times\sqrt{5}$ structural alternatives by considering the relative orientation of the dimers around the Se^{2-} monomers and the vacant site. It may be seen that in all three solutions both the monomer and vacant sites lie at the sites of the four-fold rotation axes. Therefore, the dimers surrounding each of these two sites lie either all in a tangential (or pinwheel) arrangement or in a radical (or spoke) type arrangement. We call the former orientation p and the latter s. The three $\sqrt{5}\times\sqrt{5}$ structures are therefore termed the $\sqrt{5}\times\sqrt{5}$.sp, $\sqrt{5}\times\sqrt{5}$.ps, and $\sqrt{5}\times\sqrt{5}$.pp arrangements (the first s or p in these labels refers to the geometry around the monomer site and the second label refers to that around the vacant site). The true $La_{10}Se_{19}$ structure has the $\sqrt{5}\times\sqrt{5}$.sp arrangement.

In Table 2 we list the total energy, E_{cov}, and E_{ion} for each of these structure types. As in the previous study for $LaSe_2$, both E_{cov} and E_{ion} are lowest for the experimentally observed arrangement (the $\sqrt{5}\times\sqrt{5}$.sp structure type). The reasons for these energetic results may be simply understood. We consider first the three $\sqrt{2}\times\sqrt{13}$ local minima. An examination of these three structures shows that these structures resemble the $\sqrt{2}\times\sqrt{2}$.1 and $\sqrt{2}\times\sqrt{2}$.2 structures discussed in the previous section, with the $\sqrt{2}\times\sqrt{13}$.1 structure resembling most the $\sqrt{2}\times\sqrt{2}$.1 structure and the $\sqrt{2}\times\sqrt{13}$.2 structure resembling most the $\sqrt{2}\times\sqrt{2}$.2 pattern. We recall that the $\sqrt{2}\times\sqrt{2}$.2 structure is lower in energy than the $\sqrt{2}\times\sqrt{2}$.1 pattern. As the $\sqrt{2}\times\sqrt{13}$.2 is the closest in geometry to the $\sqrt{2}\times\sqrt{2}$.2 pattern, we therefore expect it to be the lowest in energy of the three $\sqrt{2}\times\sqrt{13}$ alternatives. This is indeed the case. However, although there are good HOMO–LUMO interactions in the $\sqrt{2}\times\sqrt{13}$.1 cell, there are still energetically useless LUMO–LUMO interactions, as the Se_2^{2-} dimers of the $\sqrt{2}\times\sqrt{13}$.1 structure are coaxial.

We now turn to the $\sqrt{5}\times\sqrt{5}$ solutions. As Table 2 shows, the $\sqrt{5}\times\sqrt{5}$.sp and $\sqrt{5}\times\sqrt{5}$.pp patterns have significantly lower E_{cov} values than does the $\sqrt{5}\times\sqrt{5}$.ps pattern. We may understand this result by considering the HOMO and LUMO orbitals of the Se_2^{2-} and Se^{2-} fragments. In particular we note that there are no LUMOs for the isolated Se^{2-}. Instead, all three p-orbitals form together a degenerate set of HOMOs. To maximize HOMO–LUMO interactions, we therefore need to ensure that the sole LUMOs (which are the Se_2^{2-} σ^*-antibonding orbitals) are directly pointed toward either a Se_2^{2-} π^*-antibonding HOMO orbital or a Se^{2-} HOMO p-orbital. It may be seen in Figure 8 that this occurs only in the $\sqrt{5}\times\sqrt{5}$.sp and $\sqrt{5}\times\sqrt{5}$.pp energy minima. It is for this reason that these two structures have the lowest E_{cov} among the six minima. The chief difference between the $\sqrt{5}\times\sqrt{5}$.sp and $\sqrt{5}\times\sqrt{5}$.pp solutions lies in their ionic energies. The $\sqrt{5}\times\sqrt{5}$.sp structure is nearly 2 eV lower in energy than the $\sqrt{5}\times\sqrt{5}$.pp structure. This difference in energy is primarily caused by the difference in charge between the selenium atoms in the Se_2^{2-} dimers and the Se^{2-} monomers. The formal charges for these two types of selenium atoms are respectively –I and –II. As mentioned in the previous section, ionic energy is minimized when the anions are kept as far apart from each other as possible. In the $La_{10}Se_{19}$ structure we have both –I and –II selenium atoms. We minimize E_{ion} if we isolate the higher charged Se(–II) atoms. In the $\sqrt{5}\times\sqrt{5}$.sp pattern the atoms in the Se_2^{2-} dimers are arranged in a spoke around the Se^{2-} atom, while in the $\sqrt{5}\times\sqrt{5}$.pp pattern they are oriented in a pinwheel arrangement. In the former spoke arrangement, the distortion of the selenium atoms in the Se_2^{2-} dimers allows the Se_2^{2-} atoms to move directly away from the Se^{2-} monomer, while in the latter pinwheel arrangement the distortion is tangential with correspondingly small changes in second-nearest neighbor Se–Se bond lengths. It is for this reason that the $\sqrt{5}\times\sqrt{5}$.sp structure, experimentally observed in $La_{10}Se_{19}$, is the energetically preferred arrangement.

$RbDy_3Se_8$ Structure Type

Unlike the preceeding examples, the superstructure of the $RbDy_3Se_8$ structure has not been resolved experimentally. In this section we therefore apply the energy expressions (1) and (2) to suggest reasonable alternatives for the $RbDy_3Se_8$ superstructure. We review first the known characteristics of this structure.[5] The substructure of the $RbDy_3Se_8$ structure type has been solved to an *R*-factor of $R_w = 1.92\%$ with a unique reflection to parameter ratio of 21.4 to 1. The reported composition has been determined both by single-crystal refinement of the subcell structure and by electron microprobe. (These chemical analyses agree to within 1% of each other). The cell dimensions of the substructure are $a = 4.0579$ Å, $b = 3.8909$ Å, and $c = 26.47$ Å. This structure is illustrated in Figure 10. It is a layer structure with a distorted cubic motif of rare earth and selenium atoms interspersed with four-fold coordinate square sheets of selenium atoms. The structure closely resembles that of $NdTe_3$.[3h] As in the $NdTe_3$ structure, there are twice as many square sheets of Se atoms as there are distorted cubic layers. Unlike the case of the $NdTe_3$ structure there is a partially occupied layer of rubidium atoms between the square sheets of selenium atoms.

We base our analysis of the $RbDy_3Se_8$ structure on the following additional experimental observations. As is shown in Figure 10, there are two atoms in each square sheet in the $RbDy_3Se_8$ subcell. (Each subcell contains four of these square-sheet layers.) The two atoms in each square sheet are crystallographically inequivalent. One atom has a full occupation factor and a fairly isotropic thermal ellipsoid. The second position has a two-thirds occupation factor and can be viewed as a pair of sites approximately $^1/_2$ Å

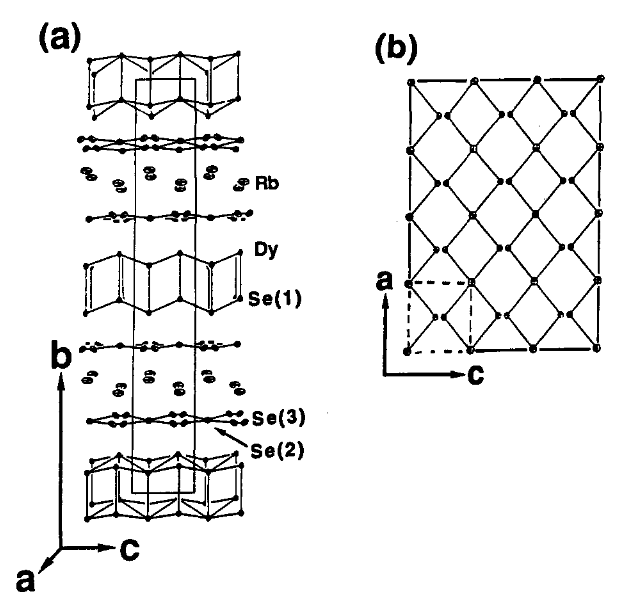

Figure 10. (a) RbDy$_3$Se$_8$ structure. (b) Subcell (dashed line) and supercell (solid line) in the selenium sheet of RbDy$_3$Se$_8$.

apart. It should be noted that this short distance of $^{1}/_{2}$ Å precludes the simultaneous occupation of both sites. In the subcell, all four square-sheet layers are crystallographically equivalent. The rubidium atom site lies only 2.1 Å away from the partially occupied square-sheet selenium sites. This distance is too short for a Rb–Se bond (in Rb$_2$Se, Rb–Se bond lengths are 3.47 Å), and we therefore conclude that for every close-lying Rb and Se pair either the rubidium site is occupied or alternatively one of the pair of Se sites is occupied. This agrees with the $^{2}/_{3}$ and $^{1}/_{3}$ occupancy factors for respectively the close Se pair and the Rb sites. Both Weissenberg and precession camera photographs show a supercell which is a factor of 3 bigger along the *b* axis. Weaker supercell reflections were also found that correspond to a quadrupling of the *a* axis. For this supercell, there are 24 selenium sites per square sheet-layer (the original two atoms per substructure square layer × a three-fold increase in *b* × a four-fold increase in *a*). Of these 24 sites, four are vacant (with a Rb atom directly above or beneath the vacant site), eight are in one of two distinct positions 0.5 Å apart, and twelve are in the original ideal position. Some counting shows that, excluding duplication by symmetry, there are 5632 ways to fulfill these above requirements. If we recall that there are four such square sheets per unit cell, even with the assumption that all four sheets have the same pattern of Se atoms, there are roughly 10^7 ways of forming a supercell compatible with the subcell data. This is a large number.

We have found, however, that it is possible to find the lowest energy patterns. We divided our calculations into the following simple steps. We considered first a single square-sheet layer of the selenium atoms with a single layer of rubidium atoms beneath it and a single distorted cubic layer of dysprosium and selenium atoms above it. We then considered a 1536 subset of the 5632 patterns.[19] From this subset we deduced that there were clear structure–energy relations which obviated the need to examine the remaining alternatives. Of these 1536 alternatives, five were clearly lower in energy than the rest. We then assumed that every square layer was crystallographically equivalent.[20] We considered the interaction between two adjacent square-sheet layers. For each of the five low-energy solutions, there were only a few stackings which had low overall energy. We chose eight such alternatives as likely candidates for the RbDy$_3$Se$_8$ superstructure.

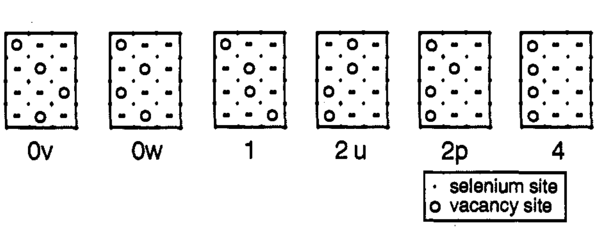

Figure 11. Several of the defect patterns for the RbDy$_3$Se$_8$ superstructure compatible with the substructure data.

In the preliminary analysis, we consider first the placement of the defect sites in a single sheet of the square Se lattice. There are four defect sites which can lie in any one of twelve positions. These twelve positions form a 3 × 4 grid (due to the three-fold increase in *b* and the four-fold increase in *a*, see Figure 10). We consider initially those defect patterns in which each row of the 3 × 4 grid contains exactly one defect site. There are six ways of distributing the four defect sites. They are illustrated in Figure 11. The names given in Figure 11 are based on the number of defect sites directly adjacent to other defect sites. To distinguish between the various alternative structures with the same number of neighboring defects, we use the roman letters v, w, u, and p (on the basis of the approximate pattern the defects make) as a second label.

For any of these structures types there are eight sites where the selenium atoms can lie in one of a pair of positions 0.5 Å apart. This leads to a total of 256 (2^8) arrangements possible for each of the six alternative lattice sites. We calculated the energy of these 1536 (6 × 256) alternatives using the method described in the previous section.[21] In reviewing the energies of the various patterns, several systematic trends were observed. First, the ionic energies of the 0v and 0w cells (these had no adjacent defect sites) were consistently lower than those for the remaining four cells. Indeed there is a direct correlation between the placing of defect sites adjacent to one another and the total ionic energy. The general rule is that for each additional pair of adjacent defect sites the overall energy increases by 2 eV. This increase in energy can be readily understood if one recalls that each defect site has a rubidium atom directly below or above it. The repulsive Coulombic rubidium–rubidium interactions are minimized when rubidium atoms are not adjacent to one another. We recall from the previous section that the known rare earth polychalcogenide superstructures correspond to energetic minima for both E_{ion} and E_{cov}. We conclude that the true superstructures, in order to minimize E_{ion}, will not contain adjacent defect sites. Arrangement other than the six types illustrated in Figure 11 all have adjacent defect sites and are thus not considered further.

We now turn to E_{cov} and E_{tot}. We find five unit cells which have significantly lower E_{cov} values than the others. These are illustrated in Figure 12, along with a sixth pattern discussed below. These six solutions belong to two sets of solutions. In the first set are the patterns labelled 0v.htcc, 0v.htpp, and 0w.htpc. In these three patterns the 20 selenium square-sheet atoms have distorted to form two V-shaped Se_3^{2-} trimers and two W-shaped Se_7^{6-} heptamers per unit cell. The h and t sublabels in the solution names refer to respectively heptamers and trimers. The meanings of the indices p and c are discussed below. For these oligomers we assign charges by assuming, in accordance with the VSEPR, that one-coordinate selenium atoms have an oxidation state of –I, two-coordinate linear selenium atoms have an oxidation state of –II, and two-coordinate bent selenium atoms have an oxidation state of zero. The total charge per 20 selenium atoms is therefore –16. This correctly balances the charges in RbDy$_3$Se$_8$ (where we

---

(19) We did not initially use the method of steepest descent optimization, as we wanted to carefully survey all possible alternatives compatible with the experimental data. Nevertheless, in our hands, the method of steepest descent optimization did produce most of the lowest energy structures.

(20) There is no prior reason to assume every layer is identical. For example in the rare earth selenide SmSe$_{1.85}$, there are two different types of selenium layers. See: Hoistad, L. Ph.D. Thesis, University of Michigan, Ann Arbor, 1993.

(21) We used Rb$_2$Se crystal data to derive the repulsive constant B of eq 1. This data was taken from ref 13.

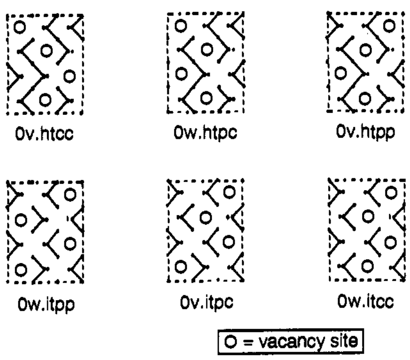

Figure 12. Local energy minimum structures for the $RbDy_3Se_8$ supercell.

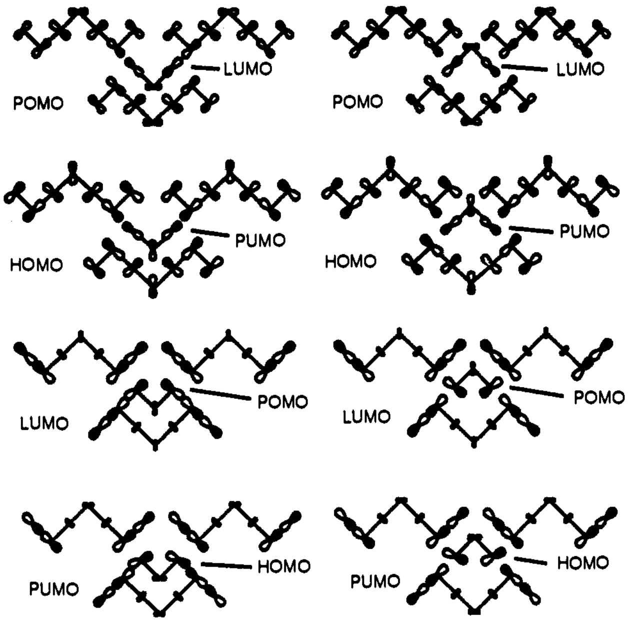

Figure 13. HOMO–LUMO diagrams comparing the two possible orientations of a Se_3^{2-} trimer in an environment of three Se_7^{6-} heptamers.

recall that three of the eight selenium atoms in the formula unit are Se(−II) atoms lying in the distorted cubic planes).[22]

The variation in E_{cov} for these supercell distortion patterns can be rationalized by analysis of HOMO–LUMO interactions as done above for $LaSe_2$ and $La_{10}Se_{19}$. For patterns of heptamers and trimers we refer back to Figure 6, where we show pertinent MO diagrams. For both heptamers and trimers, there are both symmetric and antisymmetric (with respect to a central mirror plane) HOMOs and LUMOs.

As can be seen in Figure 12 for distortion patterns with heptamers and trimers only, heptamers are always found oriented in the same way relative to each other. Different patterns are obtained by switching the orientations of the trimers with respect to the heptamer array. In Figure 13 we compare diagrammatically the HOMO–LUMO interactions for the two possible orientations of a trimer in an environment of heptamers. Strong HOMO–LUMO overlap, which would allow energetically favorable bonding interactions, is found in the diagrams on the left side of Figure 13, where trimers are pointed toward the pocket of the centered heptamer (we call this orientation "cradled" with the letter "c" added to pattern sublabels). In contrast, the diagrams on the right side of Figure 13 show a lack of significant overlap of HOMO–LUMO orbitals for the other possible orientation of the trimer. This less energetically favorable orientation has the trimer pointed away from the centered heptamer and is referred to as "peaked" with the letter "p" added to pattern sublabels. In agreement with the HOMO–LUMO diagrams, E_{cov} is minimized for the unit cell pattern with both trimers in the "cradled" orientation (Figure 12 and Table 3). The lowest energy arrangement among the three ht solutions is thus the Ov.htcc pattern. When trimers are switched to the "peaked" orientation, E_{cov} is correspondingly destabilized, as seen for Ov.htpc and Ov.htpp.

Table 3. Local Minima for Single Sheet of $RbDy_3Se_8$

type	E_{tot} (eV)	E_{cov} (eV)	E_{ion} (V)
Ov.htcc	−5282.66	−4690.76	−591.90
Ow.htpc	−5282.06	−4689.99	−592.06
Ov.htpp	−5282.02	−4689.21	−592.81
Ow.itpp	−5283.38	−4690.81	−592.57
Ov.itpc	−5282.27	−4689.91	−592.35
Ow.itcc	−5280.60	−4689.05	−591.54

Table 4. Lowest Energy Structures for $RbDy_3Se_8$

type	E_{tot} (eV)[a]	E_{cov} (eV)	E_{ion} (eV)
Ow.itpp	−10595.05	−9376.97	−1218.08
Ov.htcc	−10593.33	−9376.86	−1216.46
Ow.htpci	−10592.56	−9375.35	−1217.21
Ow.htpcii	−10592.55	−9375.35	−1217.20
Ow.htpciii	−10592.55	−9375.36	−1217.20
Ov.itpc	−10592.49	−9375.19	−1217.30
Ow.itcc	−10592.46	−9375.19	−1217.27
Ov.htpp	−10591.92	−9373.78	−1218.14

[a] Energy is per $Rb_8Dy_{24}Se_{64}$ cell.

The second family of solutions consists of Se_3^{2-} trimers and $[Se_4^{4-}]_\infty$ infinite chains. Using the label i for infinite chain, we give these structures the names Ow.itpp, and Ov.itpc and Ow.itcc. The oxidation states of the various atoms agree with the overall charge requirements of the $RbDy_3Se_8$ formula.

Again we look to HOMO–LUMO interactions to rationalize the variation in E_{cov} obtained for these patterns. We break this problem down into interactions between an infinite chain and a trimer and interactions between two trimers. In Figure 14a we show HOMO–LUMO interactions possible for trimers pointed at or away from (again referred to as "cradled" and "peaked", respectively) infinite chains. It may be seen that the overlaps for the two arrangements are roughly comparable. However, the peaked and cradled orientations do not just control the relative positions of the infinite chains to the trimers. As may be seen in Figure 12 they also control the relative orientation of the trimers to other trimers. In particular in the Ow.itcc arrangement all trimers are oriented in the same direction while in the Ow.itpp arrangement half the trimers point one way and half the trimers point the other way. We consider the interaction of the parallel vs the opposed trimers in Figure 14b. It can be seen that adjacent trimers pointed in opposite directions maximize HOMO–LUMO overlap, while adjacent trimers pointed in the same direction do not. Referring back to Figure 12 and Table 3, we note that the "it pattern" with all adjacent trimers pointing in opposite directions, Ow.itpp, is lowest in energy. When one or two trimers are switched to the "cradled" orientation (Ov.itpc and Ow.itcc), E_{cov} is correspondingly destabilized.

We now turn to the stacking of these planar networks. As may be seen in Figure 10, the square sheets lie relatively close to other sheets with only a thin layer of rubidium atoms between them. We therefore consider the interactions in these pairs of selenium square sheets. We make the assumption that both pairs of square sheets are crystallographically equivalent. This way we need to consider only a relatively small number of stackings. We find that the energies of the various alternatives are dominated by E_{ion}. The lowest energy alternatives invariably place rubidium

---

(22) Note the assignments of charge due to a VSEPR count and a molecular orbital charge density calculation need not be the same. For example, in the linear trimer Se_3^{4-}, VSEPR places a −II charge on the central Se atom and a −I charge on the peripheral Se atoms. By contrast MO calculations place a greater negative charge on the peripheral atoms.

(23) We show only orbital representations for the infinite chain at $k = \Gamma$. These are well representative, as the bands near the Fermi level are quite flat.

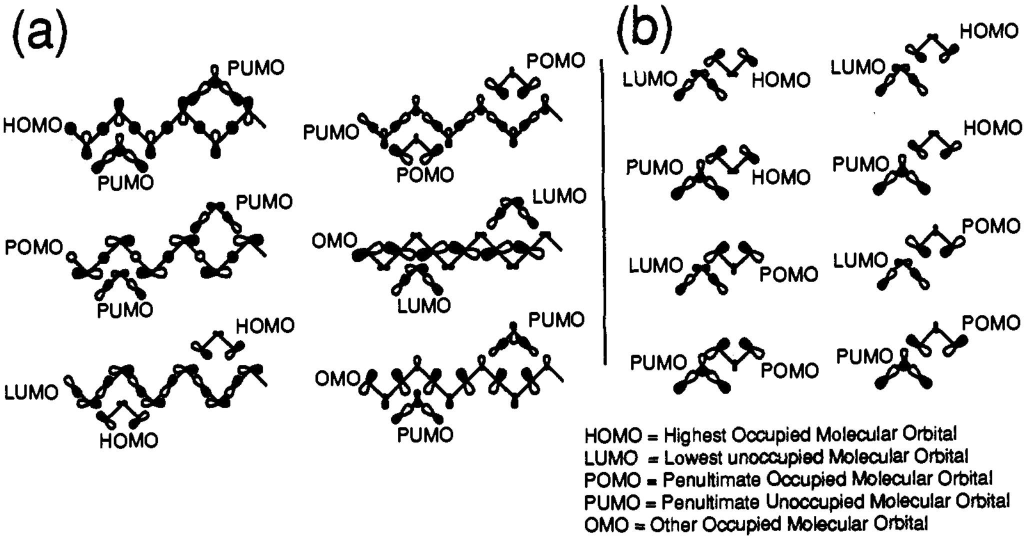

Figure 14. HOMO–LUMO diagrams comparing interactions (a) for the two possible orientations of a trimer with respect to an infinite chain and (b) for the two possible trimer–trimer orientations.[23]

atoms as far apart from one another as possible. In Table 4 we list the E_{tot}, E_{cov}, and E_{ion} for the lowest energy alternatives. 0w.htpc structures have three possible structures labeled i, ii, and iii to account for allowable shifts between neighboring selenium sheets. The actual fractional coordinates for some of these solutions are given in the supplementary material. It should be noted that we have not considered the further interaction between pairs of selenium square sheets that lie $c/2$ (13.24 Å) apart.

Acknowledgment. This research was supported by the Petroleum Research Fund, administered by the American Chemical Society. We thank the Alfred P. Sloan Foundation and the John D. and Catherine T. MacArthur Foundation for fellowships granted to S. L. Our research would not have been possible without the computer programs developed by R. Hoffmann, M.-H. Whangbo, M. Evain, T. Hughbanks, S. Wijeyesekera, M. Kertesz, C. N. Wilker, C. Zheng, J. K. Burdett, G. Miller, and T. J. McLarnan. We thank Prof. Timothy Hughbanks for his discussion on the difference between VSEPR charge assignments and charge assignments based on molecular orbital theory.

Supplementary Material Available: Tables of atomic coordinates for $RbDy_3Se_8$ 0w.itpp and $RbDy_3Se_8$ 0v.htcc (2 pages). This material is contained in many libraries on microfiche, immediately follows this article in the microfilm version of the journal, and can be ordered from the ACS; see any current masthead page for ordering information.